

The fully-implicit log-conformation formulation and its application to three-dimensional flows

Philipp Knechtges

Aachen Institute
for Advanced Study in
Computational Engineering Science

Financial support from the
Deutsche Forschungsgemeinschaft (German Research Foundation)
through grant GSC 111 is gratefully acknowledged.

The fully-implicit log-conformation formulation and its application to three-dimensional flows

Philipp Knechtges*

*Chair for Computational Analysis of Technical Systems (CATS), RWTH Aachen University, 52056 Aachen, Germany
Center for Computational Engineering Science (CCES), RWTH Aachen University, 52056 Aachen, Germany*

Abstract

The stable and efficient numerical simulation of viscoelastic flows has been a constant struggle due to the High Weissenberg Number Problem. While the stability for macroscopic descriptions could be greatly enhanced by the log-conformation method as proposed by Fattal and Kupferman, the application of the efficient Newton–Raphson algorithm to the full monolithic system of governing equations, consisting of the log-conformation equations and the Navier–Stokes equations, has always posed a problem. In particular, it is the formulation of the constitutive equations by means of the spectral decomposition that hinders the application of further analytical tools. Therefore, up to now, a fully monolithic approach could only be achieved in two dimensions, as, e.g., recently shown in [P. Knechtges, M. Behr, S. Elgeti, Fully-implicit log-conformation formulation of constitutive laws, *J. Non-Newtonian Fluid Mech.* 214 (2014) 78–87].

The aim of this paper is to find a generalization of the previously made considerations to three dimensions, such that a monolithic Newton–Raphson solver based on the log-conformation formulation can be implemented also in this case. The underlying idea is analogous to the two-dimensional case, to replace the eigenvalue decomposition in the constitutive equation by an analytically more “well-behaved” term and to rely on the eigenvalue decomposition only for the actual computation. Furthermore, in order to demonstrate the practicality of the proposed method, numerical results of the newly derived formulation are presented in the case of the sedimenting sphere and ellipsoid benchmarks for the Oldroyd-B and Giesekus models. It is found that the expected quadratic convergence of Newton’s method can be achieved.

Keywords: Log-conformation, Oldroyd-B model, Giesekus model, Finite element method
2010 MSC: 76A10, 76M10

1. Introduction

Viscoelastic flows are ubiquitous in modern industrial applications. They are essential for the correct description of the flow properties of blood, as well as polymer melts, which makes a good understanding of the used models necessary for applications ranging from the design of blood pumps [1] to the layout of extrusion dies in plastics manufacturing [2].

Considering the demands stemming from the non-linear behavior of most of the used models and, at the same time, the possibilities given through the advent of the computer age, it has become more and more common not to base the model analysis solely on pure analytic grounds, but also to perform numerical simulations, which can be applied to almost arbitrary geometries and domains. In the past, the macroscopic descriptions have been quite dominant, whereas micro-macro simulations based on stochastic differential equations are now gaining importance [3, 4]. Although the latter offer a greater flexibility with respect to the modeling of the underlying molecular dynamics, the former are still quite popular due to their

*Corresponding author

Email address: knechtges@cats.rwth-aachen.de (Philipp Knechtges)

lower computational cost. Since this is important for the application of the numerical methods to complex geometries, this paper seeks a description in the macroscopic framework. More specifically, we will consider the Oldroyd-B [5] and the Giesekus model [6]. The applicability of our methods, however, is not limited to these two models.

Simultaneously to the advent of numerical methods in the simulation of viscoelastic models, the High Weissenberg Number Problem arose [7, 3]. With the Weissenberg number being a dimensionless constant that weights the contribution of the viscoelastic equations to the description of the full system, this abstract term expresses the empirical fact that, with increasing Weissenberg number, numerical simulations tend to fail. In fact, the range of attainable Weissenberg numbers turned out to be quite often lower than what was measured in experiments, thus reducing the predictive power of simulations.

The most recent and quite successful approaches tackling the High Weissenberg Number Problem are the log-conformation methods, first considered in [8] in order to better resolve exponential stress-boundary layers in regions of high strain. Although they do not solve the High Weissenberg Number Problem completely, they address the subproblem that numerical simulations do not necessarily preserve the positive-definiteness of the conformation tensor; a property always fulfilled by the undiscretized equations [9]. The latter was found to be crucial for a numerical simulation not to fail. The underlying idea of the log-conformation methods is as simple as it is powerful: The so far primal degree of freedom — the conformation tensor σ — is replaced by its logarithm Ψ . Hence, σ is obtained by means of the matrix-exponential function $\exp \Psi$, which automatically ensures that σ remains positive-definite.

This, however, comes at the cost of finding a suitable replacement for the corresponding constitutive equation. The way the original method [8] pursues is rather unusual, compared to other partial differential equations, in the requirement of an eigenvalue decomposition of Ψ . In particular, it is this spectral decomposition that hinders the direct application of the Newton–Raphson algorithm to the full set of partial differential equations. More specifically, the Newton–Raphson method involves a determination of derivatives with respect to the Ψ degrees of freedom, including the derivatives of the eigenvalues and eigenvectors. Nevertheless, considering the derivatives of eigenvectors, it is known that they become singular in the case of degenerate eigenvalues due to the ambiguity in the eigenvectors. As a remedy for this and for the difficulty of taking the derivative of the matrix-exponential function, first attempts resorted to the approximation of the Jacobian matrix by difference quotients [10, 11].

Even though a first analysis was conducted for the two-dimensional Leonov model in [12], it was not until the work in [13] and [14] that the Jacobian matrix was derived by pure analytic means in two dimensions for a broader class of models. As a continuation of these earlier works, this paper is devoted to a generalization to arbitrary dimensions, along which we will also bridge the gap between the two expositions in [13] and [14].

In particular, we will not only discuss the derivation of a new constitutive equation in the first section, but also describe the numerical implications in the case of an implementation into an existing Galerkin/Least-Squares (GLS) Navier–Stokes solver in the succeeding section. The results of this solver are subsequently used in Section 4 to study the falling sphere benchmark, where a sphere of radius R sediments along the centerline of a tube of radius $2R$. In order to demonstrate the applicability to truly three-dimensional flows, a modification of the same benchmark with a tri-axial ellipsoid is considered as well.

Although our motivation stems mostly from the numerical side, the proposed equations are purely analytic and as such may also serve as a new tool in future analytic studies; to the author’s knowledge, this is the first time that the constitutive equations for the log-conformation formulation can be stated in a closed form in this generality.

2. Theory

The aim of this section is the derivation of an alternative constitutive equation with Ψ as a new primal variable. Starting point is the original constitutive equation in terms of the conformation tensor σ and the velocity \mathbf{u} . Both are fields that, given boundary and initial conditions, have to be determined over a time-span $[0, T]$ and a d -dimensional domain $\tilde{\Omega} \subset \mathbb{R}^d$.

Following the exposition in [13], we consider constitutive models of the form

$$\partial_t \boldsymbol{\sigma} + (\mathbf{u} \cdot \nabla) \boldsymbol{\sigma} + [\boldsymbol{\sigma}, \Omega(\mathbf{u})] - \varepsilon(\mathbf{u}) \boldsymbol{\sigma} - \boldsymbol{\sigma} \varepsilon(\mathbf{u}) = -\frac{1}{\lambda} P(\boldsymbol{\sigma}), \quad (1)$$

where $\varepsilon(\mathbf{u}) = \frac{1}{2} (\nabla \mathbf{u} + \nabla \mathbf{u}^T)$ denotes the strain tensor, $\Omega(\mathbf{u}) = \frac{1}{2} (\nabla \mathbf{u} - \nabla \mathbf{u}^T)$ the vorticity tensor, λ the relaxation time, and $P(\boldsymbol{\sigma})$ an analytic function. The bracket $[\boldsymbol{\sigma}, \Omega(\mathbf{u})]$ is the so-called commutator, which is defined as

$$[\boldsymbol{\sigma}, \Omega(\mathbf{u})] = \boldsymbol{\sigma} \Omega(\mathbf{u}) - \Omega(\mathbf{u}) \boldsymbol{\sigma}.$$

Common choices for $P(\boldsymbol{\sigma})$ are $P(\boldsymbol{\sigma}) = \boldsymbol{\sigma} - \mathbf{1}$, leading to the Oldroyd-B model [5], or $P(\boldsymbol{\sigma}) = \boldsymbol{\sigma} - \mathbf{1} + \alpha(\boldsymbol{\sigma} - \mathbf{1})^2$ with $\alpha \in [0, 1]$ in the Giesekus model [6]. Generalizations of the subsuming methods to the Johnson-Segalman model, as, e.g., done in [14], or other models are in principle possible, but omitted here for the sake of brevity.

Since the velocity field \mathbf{u} is not determined so far, we have to combine the constitutive equations with the Navier–Stokes equations in order to obtain a complete system of partial differential equations. More specifically, the Navier–Stokes equations are given by

$$\begin{aligned} \nabla \cdot \mathbf{u} &= 0 \\ \rho(\partial_t + \mathbf{u} \cdot \nabla) \mathbf{u} + \nabla p - 2\mu_S \nabla \cdot \varepsilon(\mathbf{u}) - \frac{\mu_P}{\lambda} \nabla \cdot (\boldsymbol{\sigma} - \mathbf{1}) &= 0, \end{aligned} \quad (2)$$

with density ρ , as well as solvent and polymeric viscosity constants μ_S and μ_P , respectively.

Furthermore, we will introduce function spaces \mathcal{H} and \mathcal{H}' , which for the moment could be chosen as perfectly smooth, i.e., $\mathcal{H} = \mathcal{H}' = C^\infty([0, T] \times \overline{\Omega})$, and the derived spaces

$$\begin{aligned} H &= \mathcal{H}^{d \times d} & H_{sym} &= \{X \in H \mid X^T = X\}, \\ H' &= \mathcal{H}'^{d \times d} & H'_{sym} &= \{X \in H' \mid X^T = X\}. \end{aligned}$$

The central statement of this paper then reads:

Theorem 1. *Let the velocity field \mathbf{u} be given with $\varepsilon(\mathbf{u}) \in H'_{sym}$ and $\Omega(\mathbf{u}) \in H'$. If $\Psi \in H_{sym}$ satisfies*

$$\partial_t \Psi + (\mathbf{u} \cdot \nabla) \Psi + [\Psi, \Omega(\mathbf{u})] - \frac{1}{(2\pi i)^2} \int_\Gamma \int_\Gamma f(z - z') \frac{1}{z - \Psi} \varepsilon(\mathbf{u}) \frac{1}{z' - \Psi} dz dz' = -\frac{1}{\lambda} P(e^\Psi) e^{-\Psi} \quad (3)$$

with

$$f(x) = x + \frac{2x}{e^x - 1} = \frac{x}{\tanh(x/2)},$$

and Γ chosen as a closed path surrounding the spectrum of Ψ in $\{z \in \mathbb{C} \mid |\operatorname{Im}(z)| < \pi\}$, then $\boldsymbol{\sigma} = \exp \Psi \in H_{sym}$ solves the original constitutive equation (1).

Before we come to the proof of this theorem, we need to consider certain properties of the relevant terms. The first thing to notice in Eq. (3) is the double integral, which is similar to the familiar Cauchy integral from complex analysis. One of the main differences to the ordinary Cauchy integral, however, is that the scalar ratio has been replaced by the resolvent $1/(z - \Psi) := (z\mathbf{1} - \Psi)^{-1}$, where $\mathbf{1}$ is the identity matrix and $^{-1}$ indicates the matrix inverse. For smooth function spaces, it can be deduced that, at a specific instant of space and time, the resolvent exists if and only if z does not equal any of the eigenvalues of $\Psi(t, \mathbf{x})$, which are all real-valued. Encircling these poles with our integration path Γ subsequently gives us, by the same means as in the Cauchy integral setting, some information on f at these poles, but with the additional complexity that we have to deal with the matrix algebra.

Although we will further use this idea of numerically evaluating the integrals at the eigenvalues later on, we will now leave the setting of smooth function spaces. Instead, we consider the more general case of

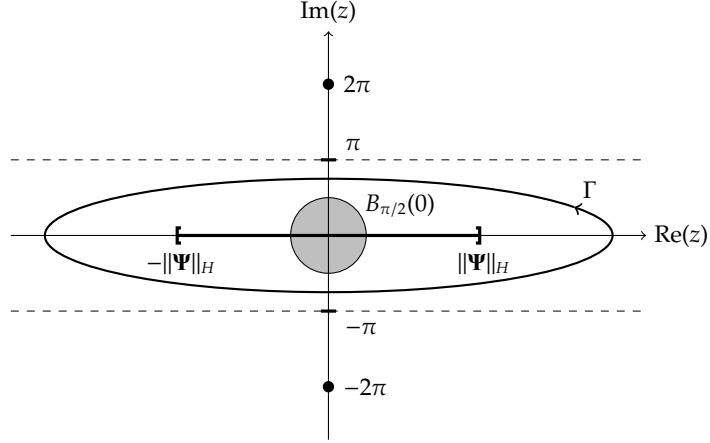


Figure 1: Illustration of a particular choice of the integration path Γ , as used in Theorem 1. Here, choosing Γ as an ellipse, with semi-major axis greater than $\|\Psi\|_H$ and semi-minor axis smaller than π , ensures that the spectrum of Ψ is enclosed by Γ , while the poles of f , especially $\pm 2\pi i$, do not contribute to the integral.

choosing \mathcal{H}' as a Banach space and $\mathcal{H} \subset \mathcal{H}'$ as a commutative Banach algebra. This opens up the door to a variety of spaces as they are used in the analysis of partial differential equations. An example set of spaces in this more general setting would be the Sobolev-based spaces

$$\begin{aligned} \mathcal{H} &= C^1([0, T], H^{s-1}(\tilde{\Omega})) \cap C^0([0, T], H^s(\tilde{\Omega})), \\ \mathcal{H}' &= C^0([0, T], H^{s-1}(\tilde{\Omega})), \end{aligned}$$

with $s > d/2$ and $\tilde{\Omega} \subset \mathbb{R}^d$ being a Lipschitz-bounded domain [15]. It should be stressed that the mathematical discussion here is not limited to these spaces, and for the general requirements on \mathcal{H} and \mathcal{H}' we refer to the appendix of [13].

Considering whether on these general spaces the double integral is well defined, the set of values for which the resolvent is not defined is no longer restricted to the distinct eigenvalues, but may in fact be larger, although still real-valued. Therefore, in order to separate the terminology from the matrix algebra, this set is called spectrum in the general Banach algebra setting. The generalization of Cauchy's integral to the theory of Banach algebras¹ is known as Dunford's integral and it is the essential ingredient to define a functional calculus of holomorphic functions on these algebras [16, 17]. More specifically, for a function g that is holomorphic in the neighborhood of the spectrum of Ψ , the H -valued function is defined as

$$g(\Psi) := \frac{1}{2\pi i} \int_{\Gamma} \frac{g(z)}{z - \Psi} dz, \quad (4)$$

where Γ is a contour surrounding the spectrum of Ψ within the same neighborhood. Here, as well as in Theorem 1, it is assumed that Γ encircles the spectrum only once. An immediate consequence of this definition is that it allows us to explain the exponential function of Ψ , which also has to be an element of H_{sym} .

A discrepancy between the integral in Theorem 1 and the usual Dunford integral is that the argument of f depends on the difference between the two integral variables z and z' . The latter is also what makes it more difficult to ensure that the poles of f , especially $\pm 2\pi i$, do not contribute to the integral. In the formulation of Theorem 1 this has been realized by restricting the imaginary part of the integration path Γ to the region $|\operatorname{Im} z| < \pi$. An example of a closed curve Γ fulfilling the aforementioned criteria is depicted in Fig. 1, where

¹Throughout this paper we deliberately use the same symbol for the Banach algebra as for its complexification.

the fact is also used that the spectrum of Ψ is always contained in the interval $[-\|\Psi\|_H, \|\Psi\|_H]$.

Despite this minor restriction, most of the properties of Dunford's integral carry over to the double integral as well. One of the more important features is the independence of the integral on the exact contour of Γ , which is a key consequence of Cauchy's theorem [16, Theorem 3.31].

The final reason for not including the poles of f in the integral in Theorem 1 is that we want to express f by a Taylor series in the course of the proof.

Lemma 1. *Let g be a holomorphic function on a convex domain $\Omega' \subset \mathbb{C}$. Moreover, let the ball of radius r , $B_r(0)$, be contained in Ω' . The Taylor series on this ball shall be given by $g(z) = \sum_{n=0}^{\infty} b_n z^n$. Then for every $\mathbf{A} \in H$ with $\|\mathbf{A}\|_H < r/2$, $\mathbf{B} \in H'$, and $\Gamma \subset \frac{1}{2}\Omega'$ a contour around the spectrum of \mathbf{A} , it holds*

$$\begin{aligned} F(\mathbf{A}, \mathbf{B}) &:= \frac{1}{(2\pi i)^2} \int_{\Gamma} \int_{\Gamma} g(z - z') \frac{1}{z - \mathbf{A}} \mathbf{B} \frac{1}{z' - \mathbf{A}} dz dz' \\ &= \sum_{n=0}^{\infty} b_n \{\mathbf{A}, \mathbf{B}\}_n, \end{aligned}$$

where $\{\mathbf{A}, \mathbf{B}\}_n$ denotes the n -th iterated commutator

$$\{\mathbf{A}, \mathbf{B}\}_n := [\mathbf{A}, \{\mathbf{A}, \mathbf{B}\}_{n-1}] = \sum_{i=0}^n \binom{n}{i} (-1)^i \mathbf{A}^{n-i} \mathbf{B} \mathbf{A}^i.$$

Proof. Without loss of generality, Cauchy's theorem allows us to choose a contour Γ within $B_{r/2}(0)$ that still surrounds the spectrum of \mathbf{A} . Since the Taylor series converges uniformly on every compact subset of $B_r(0)$, and especially on $\Gamma - \Gamma \subset B_r(0)$, one can deduce by similar means as for Dunford's integral (cf. [16, Theorem 10.27]) that g in $F(\mathbf{A}, \mathbf{B})$ can be approximated by the Taylor series to yield an arbitrarily accurate approximation of $F(\mathbf{A}, \mathbf{B})$. As such, we can assume $g(z - z') = (z - z')^n$. Furthermore, using a binomial expansion $(z - z')^n = \sum_{i=0}^n \binom{n}{i} (-1)^i z^{n-i} z'^i$ we obtain

$$\begin{aligned} &\frac{1}{(2\pi i)^2} \int_{\Gamma} \int_{\Gamma} g(z - z') \frac{1}{z - \mathbf{A}} \mathbf{B} \frac{1}{z' - \mathbf{A}} dz dz' \\ &= \sum_{i=0}^n \binom{n}{i} (-1)^i \left(\frac{1}{2\pi i} \int_{\Gamma} \frac{z^{n-i}}{z - \mathbf{A}} dz \right) \mathbf{B} \left(\frac{1}{2\pi i} \int_{\Gamma} \frac{z'^i}{z' - \mathbf{A}} dz' \right), \end{aligned}$$

which together with (4), or more rigorously [16, Lemma 10.24], yields the desired iterated commutator

$$= \sum_{i=0}^n \binom{n}{i} (-1)^i \mathbf{A}^{n-i} \mathbf{B} \mathbf{A}^i = \{\mathbf{A}, \mathbf{B}\}_n.$$

□

This lemma is already sufficient to prove Theorem 1 in the case $\|\Psi\|_H < \pi$, as can be seen by choosing $g(z) = f(z) = 2 \sum_{n=0}^{\infty} \frac{B_{2n}}{(2n)!} z^{2n}$, as well as $\Omega' = \mathbb{R} + i(-2\pi, 2\pi)$ and $r = 2\pi$. Then it becomes apparent that if Ψ fulfills Eq. (3), it also has to fulfill

$$\partial_t \Psi + (\mathbf{u} \cdot \nabla) \Psi + [\Psi, \Omega(\mathbf{u})] - 2 \sum_{n=0}^{\infty} \frac{B_{2n}}{(2n)!} \{\Psi, \varepsilon(\mathbf{u})\}_{2n} = -\frac{1}{\lambda} P(e^{\Psi}) e^{-\Psi},$$

where B_{2n} denote the even Bernoulli numbers. This is exactly the equation for which the conclusion in Theorem 1 has been proven in [13, Theorem 1].

The generalization to $\|\Psi\|_H \geq \pi$ is part of the

Proof of Theorem 1. Assuming Ψ solves Eq. (3), in a first step the Wilcox Lemma [18] is applied to handle the derivatives $\partial_t + \mathbf{u} \cdot \nabla$ of the exponential mapping $\sigma = \exp \Psi$, such that subsequently (3) can be inserted:

$$\begin{aligned} (\partial_t + \mathbf{u} \cdot \nabla) \sigma &= \int_0^1 e^{(1-\alpha)\Psi} ((\partial_t + \mathbf{u} \cdot \nabla) \Psi) e^{\alpha\Psi} d\alpha \\ &= -\frac{1}{\lambda} \int_0^1 e^{(1-\alpha)\Psi} P(e^\Psi) e^{-\Psi} e^{\alpha\Psi} d\alpha \\ &\quad - \int_0^1 e^{(1-\alpha)\Psi} [\Psi, \Omega(\mathbf{u})] e^{\alpha\Psi} d\alpha \\ &\quad + \int_0^1 e^{(1-\alpha)\Psi} \frac{1}{(2\pi i)^2} \int_\Gamma \int_\Gamma f(z-z') \frac{1}{z-\Psi} \varepsilon(\mathbf{u}) \frac{1}{z'-\Psi} dz dz' e^{\alpha\Psi} d\alpha. \end{aligned}$$

The integral involving $P(e^\Psi)$ is the easiest to handle since all involved terms commute with each other, resulting in the contribution $-\frac{1}{\lambda} P(\sigma)$. The vorticity term can be simplified by the fundamental theorem of calculus, which yields

$$- \int_0^1 e^{(1-\alpha)\Psi} [\Psi, \Omega(\mathbf{u})] e^{\alpha\Psi} d\alpha = \int_0^1 \partial_\alpha (e^{(1-\alpha)\Psi} \Omega(\mathbf{u}) e^{\alpha\Psi}) d\alpha = -e^\Psi \Omega(\mathbf{u}) + \Omega(\mathbf{u}) e^\Psi = -[\sigma, \Omega(\mathbf{u})].$$

Hence, for σ to fulfill the original constitutive equation it is left to prove

$$\int_0^1 e^{(1-\alpha)\Psi} \frac{1}{(2\pi i)^2} \int_\Gamma \int_\Gamma f(z-z') \frac{1}{z-\Psi} \varepsilon(\mathbf{u}) \frac{1}{z'-\Psi} dz dz' e^{\alpha\Psi} d\alpha = \varepsilon(\mathbf{u}) e^\Psi + e^\Psi \varepsilon(\mathbf{u}).$$

Rather than directly proving this equality we will follow the argumentation of Theorem 2 in [13], and consider a slightly more general equation where Ψ is replaced by $\beta\Psi$, such that an analytic continuation argument in β can be used to bridge the gap to the case $\|\Psi\|_H < \pi$. In particular, without loss of generality we will assume that Γ , in addition to the spectrum of Ψ , also encloses $B_{\pi/2}(0)$, as, e.g., depicted in Fig. 1. Our assertion now reads that

$$\int_0^1 e^{(1-\alpha)\beta\Psi} F(\beta\Psi, \varepsilon(\mathbf{u})) e^{\alpha\beta\Psi} d\alpha = \varepsilon(\mathbf{u}) e^{\beta\Psi} + e^{\beta\Psi} \varepsilon(\mathbf{u}) \quad (5)$$

shall hold with

$$F(\beta\Psi, \varepsilon(\mathbf{u})) := \frac{1}{(2\pi i)^2} \int_\Gamma \int_\Gamma f(z-z') \frac{1}{z-\beta\Psi} \varepsilon(\mathbf{u}) \frac{1}{z'-\beta\Psi} dz dz'$$

for every β in a sufficiently small simply-connected neighborhood D of $[0, 1] \cup B_{\pi/(2\|\Psi\|_H)}(0) \subset \mathbb{C}$.

It is clear that the right-hand side of Eq. (5) is holomorphic for all β , due to

$$\partial_\beta e^{\beta\Psi} = \Psi e^{\beta\Psi}.$$

Additionally, using

$$\partial_\beta \frac{1}{z-\beta\Psi} = -\frac{1}{z-\beta\Psi} \Psi \frac{1}{z-\beta\Psi}, \quad (6)$$

it is evident that the left-hand side is holomorphic for $\beta \in D$.

Restricting ourselves for a moment to $|\beta| < \pi/(2\|\Psi\|_H)$, we deduce from Lemma 1 that

$$\int_0^1 e^{(1-\alpha)\beta\Psi} F(\beta\Psi, \varepsilon(\mathbf{u})) e^{\alpha\beta\Psi} d\alpha = \int_0^1 e^{(1-\alpha)\beta\Psi} \left(2 \sum_{n=0}^{\infty} \frac{B_{2n}}{(2n)!} \{\beta\Psi, \varepsilon(\mathbf{u})\}_{2n} \right) e^{\alpha\beta\Psi} d\alpha,$$

which is essentially the form for which the identity (5) has already been proven in the proof of Theorem 2 in [13]. Thus, we are left with applying the monodromy theorem that asserts the uniqueness of the analytic continuation on D . Thereby, (5) has in particular to hold for $\beta = 1$, and σ solves the original constitutive equation (1). \square

3. Numerical implementation

Given the newly derived constitutive equation (3), we are going to discuss the numerical discretization in conjunction with the Finite Element Method (FEM). The first part of this section will be centered around the formulation of the discretized weak form in terms of space-time elements. The second part will then be concerned with the linearization of the discretized weak form by means of the Newton–Raphson method. In particular, it will also deal with the evaluation of the double integral and its derivatives. It should be noted that the two subsections are only loosely coupled and that the discussion of the latter subsection is not limited to the discretization scheme we have chosen, but may be easily generalized to other schemes.

3.1. Discretization

As in the preceding paper [13], we will use a mixture of a Streamline Upwind/Petrov-Galerkin (SUPG)- and Galerkin/Least-Squares (GLS)-stabilized finite element method in combination with space-time meshes to discretize the full monolithic system of constitutive equation (3) and Navier–Stokes equations (2). The SUPG method, which has originally been proposed in [19], will serve as the stabilization method of the advection-dominated constitutive equation, whereas a modified adjoint GLS will be used to stabilize the momentum equation [20, 21, 22]. The choice of a space-time method is mainly motivated by future applications to deforming-domain problems.

Assuming a slicing of our space-time domain Q into N slices Q_n , each spanning the computational domain from t_n to t_{n+1} , and furthermore a triangulation of Q_n by the elements collected in $\mathcal{T}_{h,n}$, we introduce the function space

$$V_{h,n} = \left\{ v \in C^0(\overline{Q_n}) \mid \forall Q_n^e \in \mathcal{T}_{h,n}, v \circ T_{Q_n^e} \in \mathbb{P}_2 \otimes \mathbb{P}_1 \right\}.$$

Here, the Lagrange elements \mathbb{P}_2 and \mathbb{P}_1 are employed in space and time, respectively, with $T_{Q_n^e}$ denoting the isoparametric geometrical mapping from the reference element onto Q_n^e . For all applications within this paper the complete space-time domain simplifies to $Q = [0, T] \times \tilde{\Omega}$ and the corresponding slices to $Q_n = [t_n, t_{n+1}] \times \tilde{\Omega}$.

Furthermore, defining the spatial boundary of the space-time slab as $P_n = \bigcup_{t \in [t_n, t_{n+1}]} \{t\} \times \partial\tilde{\Omega}_t$, where $\tilde{\Omega}_t$ designates the spatial extent of the computational domain at a given instant of time t , we use the following trial and test spaces

$$\mathcal{S}_{h,n} = \left\{ (\mathbf{u}, p, \Psi) \in (V_{h,n})^d \times V_{h,n} \times (V_{h,n})^{d \cdot (d+1)/2} \mid \mathbf{u}|_{P_{n,u}} = \mathbf{g}_u, \Psi|_{P_{n,\Psi}} = \mathbf{g}_\Psi \right\} \quad (7)$$

$$\mathcal{V}_{h,n} = \left\{ (\mathbf{v}, q, \Phi) \in (V_{h,n})^d \times V_{h,n} \times (V_{h,n})^{d \cdot (d+1)/2} \mid \mathbf{v}|_{P_{n,u}} = 0, \Phi|_{P_{n,\Psi}} = 0 \right\}, \quad (8)$$

with $P_{n,u}$ and $P_{n,\Psi}$ being the subsets of P_n on which \mathbf{g}_u and \mathbf{g}_Ψ are prescribed as Dirichlet boundary conditions. The full trial space, spanning the whole space-time domain, is hence chosen as

$$\mathcal{S}_h = \left\{ (\mathbf{u}, p, \Psi) \in L^2(Q, \mathbb{R}^{d+1+d \cdot (d+1)/2}) \mid (\mathbf{u}, p, \Psi)|_{[t_n, t_{n+1}]} \in \mathcal{S}_{h,n} \right\}.$$

Using these definitions, the discretized weak problem can be formulated as follows: *Given the initial conditions $(\mathbf{u}^h)_0^- = \mathbf{u}_0$ and $(\Psi^h)_0^- = \Psi_0$, we seek $\mathbf{z}^h = (\mathbf{u}^h, p^h, \Psi^h) \in \mathcal{S}_h$ such that on each time slab Q_n with $0 \leq n \leq N - 1$ and for every $\mathbf{w}^h = (\mathbf{v}^h, q^h, \Phi^h) \in \mathcal{V}_{h,n}$ the following equation is fulfilled:*

$$\begin{aligned}
0 = a_n(\mathbf{w}^h, \mathbf{z}^h) := & \int_{Q_n} \mathbf{v}^h \cdot \rho (\partial_t \mathbf{u}^h + (\mathbf{u}^h \cdot \nabla) \mathbf{u}^h) + \int_{Q_n} \frac{\mu_P}{\lambda} \varepsilon(\mathbf{v}^h) : (e^{\Psi^h} - \mathbf{1}) \\
& + \int_{Q_n} 2\mu_s \varepsilon(\mathbf{v}^h) : \varepsilon(\mathbf{u}^h) - \int_{Q_n} (\nabla \cdot \mathbf{v}^h) p^h + \int_{\tilde{\Omega}_n} (\mathbf{v}^h)_n^+ \cdot \rho ((\mathbf{u}^h)_n^+ - (\mathbf{u}^h)_n^-) \\
& + \sum_e \int_{Q_n^e} \tau_{mom} \frac{1}{\rho} \left(\rho (\mathbf{u}^h \cdot \nabla) \mathbf{v}^h + \nabla q^h + \mu_s \Delta \mathbf{v}^h - \frac{\mu_P}{\lambda} \nabla \cdot \Phi^h \right) \\
& \quad \cdot \left(\rho (\partial_t \mathbf{u}^h + (\mathbf{u}^h \cdot \nabla) \mathbf{u}^h) + \nabla p^h - \mu_s \Delta \mathbf{u}^h - \frac{\mu_P}{\lambda} \nabla \cdot (e^{\Psi^h} - \mathbf{1}) \right) \\
& + \int_{Q_n} q^h (\nabla \cdot \mathbf{u}^h) + \int_{\tilde{\Omega}_n} (\Phi^h)_n^+ : \frac{\mu_P}{2\lambda} ((\Psi^h)_n^+ - (\Psi^h)_n^-) \\
& + \int_{Q_n} \frac{\mu_P}{2\lambda} (\Phi^h + \tau_{cons} (\mathbf{u}^h \cdot \nabla) \Phi^h) \\
& \quad : \left(\partial_t \Psi^h + (\mathbf{u}^h \cdot \nabla) \Psi^h + [\Psi^h, \Omega(\mathbf{u}^h)] - F(\Psi^h, \varepsilon(\mathbf{u}^h)) + \frac{1}{\lambda} P(e^{\Psi^h}) e^{-\Psi^h} \right). \tag{9}
\end{aligned}$$

The inner product $\Phi : \Psi$ is as usual defined as $\text{tr}(\Phi^T \Psi)$. This weak form also incorporates concepts which are typical for space-time GLS realization, e.g., the weak coupling between the space-time slabs motivated by Discontinuous Galerkin methods. Here, $(\mathbf{u}^h)_n^\pm$ is used as the short form for $\lim_{\xi \rightarrow 0} \mathbf{u}^h(t_n \pm \xi, \cdot)$ and $\tilde{\Omega}_n = \tilde{\Omega}_{t_n}$.

Furthermore, for all subsequent calculations within this paper the stabilization parameters were chosen as

$$\begin{aligned}
\tau_{mom} &= \min \left(\rho \frac{h^2}{600 \mu}, \frac{h}{2|\mathbf{u}|}, \frac{\Delta t}{2} \right), \\
\tau_{cons} &= \min \left(\left(2 \frac{|\mathbf{u}|}{h} + \lambda^{-1} \right)^{-1}, \frac{\Delta t}{2} \right),
\end{aligned}$$

where Δt is the time-step size, h the element diameter, $\mu = \mu_s + \mu_p$ the full viscosity, and $|\mathbf{u}|$ the absolute value of the velocity evaluated at the element center. In cases where stationary simulations were performed, the corresponding parts of the discretized weak form, namely, the explicit time-derivatives as well as the discontinuous coupling across space-time slabs, were neglected, which also applies to the $\Delta t/2$ part of the stabilization constants. Similarly, in the creeping flow limit ($Re = 0$) the advective derivative of the velocity $(\mathbf{u}^h \cdot \nabla) \mathbf{u}^h$ was omitted from the momentum equation in conjunction with dropping $h/(2|\mathbf{u}|)$ from τ_{mom} .

3.2. Linearization and evaluation

In a last step, the discretized weak form (9) has to be linearized in order to make it amenable to linear solvers. As already mentioned in the introduction, the used linearization method in this work is the Newton–Raphson algorithm, which promises quadratic convergence at the additional cost of providing a variational directional derivative of the weak form. More specifically, denoting the directional derivative by

$$Da_n(\mathbf{w}^h, \cdot) \Big|_{\mathbf{z}_{n,i}^h} \delta \mathbf{z}_{n,i}^h = \frac{d}{d\xi} \Big|_{\xi=0} a_n(\mathbf{w}^h, \mathbf{z}_{n,i}^h + \xi \cdot \delta \mathbf{z}_{n,i}^h),$$

we iteratively solve

$$Da_n(\mathbf{w}^h, \cdot) \Big|_{\mathbf{z}_{n,i}^h} \delta \mathbf{z}_{n,i}^h = -a_n(\mathbf{w}^h, \mathbf{z}_{n,i}^h) \quad \forall \mathbf{w}^h \in \mathcal{V}_{h,n}$$

for $\delta z_{n,i}^h \in \mathcal{V}_{h,n}$. The updated solution $z_{n,i+1}^h$ can then be computed as $z_{n,i+1}^h = z_{n,i}^h + \delta z_{n,i}^h$. The iteration is terminated as usual when the Euclidean norm of the residual $\|\mathbf{r}\|_2 := \|a_n(\cdot, z_{n,i}^h)\|_2$ becomes smaller than a given threshold.

When the Newton–Raphson algorithm is employed in the context of the newly derived constitutive equation (3), the immediate numerical implementation may lead to difficulties: Due to their invariance on the exact contour of Γ , the evaluation of Cauchy-type integrals is prone to cancellation. This applies to the double integral as well as to the exponential mapping. The difficulty can be alleviated in the numerical setting by evaluating the integral directly or indirectly (e.g., through a quadrature rule) only at specific instants of space and time. This condenses our Banach algebra to the usual matrix algebra, which essentially implies that the spectrum of $\Psi^h(t, \mathbf{x})$ contains at most up to d distinct discrete points, i.e., the eigenvalues of $\Psi^h(t, \mathbf{x})$. Using the same techniques as are applied to identify the usual spectral decomposition method of interpreting matrix functions with the Cauchy-type definition of matrix functions (4), we will be able to reformulate the integral in the framework of eigenvalues and eigenvectors.

For this, we introduce a set of d eigenvalues λ_i and d eigenvectors $\tilde{\mathbf{e}}_i$ of $\Psi^h(t, \mathbf{x})$, which are associated to a projection operator $\mathbf{P}_i = \tilde{\mathbf{e}}_i \tilde{\mathbf{e}}_i^T$ that projects onto the one-dimensional subspaces spanned by the corresponding eigenvector. Using this notation, linear algebra states that

$$\frac{1}{z - \Psi^h} = \sum_{i=1}^d \frac{1}{z - \lambda_i} \mathbf{P}_i \quad (10)$$

has to hold, where for the sake of brevity the function arguments (t, \mathbf{x}) have been dropped. Applying this equation to the double integral simplifies it to

$$\begin{aligned} F(\Psi^h, \varepsilon(\mathbf{u}^h)) &= \frac{1}{(2\pi i)^2} \int_{\Gamma} \int_{\Gamma} f(z - z') \frac{1}{z - \Psi^h} \varepsilon(\mathbf{u}^h) \frac{1}{z' - \Psi^h} dz dz' \\ &= \sum_{i,j=1}^d \mathbf{P}_i \varepsilon(\mathbf{u}^h) \mathbf{P}_j \frac{1}{(2\pi i)^2} \int_{\Gamma} \int_{\Gamma} f(z - z') \frac{1}{z - \lambda_i} \frac{1}{z' - \lambda_j} dz dz', \end{aligned}$$

which then together with Cauchy's integral formula (or the residue theorem) yields

$$F(\Psi^h, \varepsilon(\mathbf{u}^h)) = \sum_{i,j=1}^d f(\lambda_i - \lambda_j) \mathbf{P}_i \varepsilon(\mathbf{u}^h) \mathbf{P}_j. \quad (11)$$

It should be noted that this is the form of the $\varepsilon(\mathbf{u})$ -term in the constitutive equation as it has been considered in [14].

Of course, there is no doubt that, with the numerically well-studied QR-algorithms in mind, this form is much more suitable for numerical evaluation. Nonetheless, it falls short in many applications when it comes to study perturbations of Ψ^h , as it is the case for the variational derivative needed in the Newton-Raphson algorithm. Existing implementations, as, e.g., in [13, 14], were limited to the two-dimensional case, since for a 2×2 matrix it is still feasible to derive an algebraic closed expression for eigenvalues and eigenvectors in dependence of Ψ^h . Another approach would be general perturbation theory [23], which directly applies to eigenvalues λ_i and their projection operators \mathbf{P}_i , but this theory is prone to singularities in the vicinity of degenerate eigenvalues.

The solution we will pursue here is similar to the general perturbation method in means of using complex calculus. As such we perform the perturbation first in the framework of the double integral and then switch to the eigenvalue representation. E.g., considering the variational derivative of the double integral $F(\Psi, \varepsilon(\mathbf{u}))$

with respect to Ψ^h in the direction $\delta\Psi^h$, one obtains by similar means as in Eq. (6)

$$\begin{aligned} \frac{\partial}{\partial \xi} \Big|_{\xi=0} F(\Psi^h + \xi \delta\Psi^h, \varepsilon(\mathbf{u}^h)) &= \frac{1}{(2\pi i)^2} \int_{\Gamma} \int_{\Gamma} f(z-z') \frac{1}{z-\Psi^h} \delta\Psi^h \frac{1}{z-\Psi^h} \varepsilon(\mathbf{u}^h) \frac{1}{z'-\Psi^h} dz dz' \\ &+ \frac{1}{(2\pi i)^2} \int_{\Gamma} \int_{\Gamma} f(z-z') \frac{1}{z-\Psi^h} \varepsilon(\mathbf{u}^h) \frac{1}{z'-\Psi^h} \delta\Psi^h \frac{1}{z'-\Psi^h} dz dz'. \end{aligned}$$

Inserting Eq. (10) and applying the residue theorem then yields

$$\frac{\partial}{\partial \xi} \Big|_{\xi=0} F(\Psi^h + \xi \delta\Psi^h, \varepsilon(\mathbf{u}^h)) = \sum_{i,j,k=1}^d \frac{f(\lambda_i - \lambda_k) - f(\lambda_j - \lambda_k)}{\lambda_i - \lambda_j} (\mathbf{P}_i \delta\Psi^h \mathbf{P}_j \varepsilon(\mathbf{u}^h) \mathbf{P}_k + \mathbf{P}_k \varepsilon(\mathbf{u}^h) \mathbf{P}_j \delta\Psi^h \mathbf{P}_i), \quad (12)$$

where in accordance with the residue theorem the difference quotient has to be replaced by $f'(\lambda_i - \lambda_k)$ if λ_i and λ_j coincide. It is clear that this formula can be evaluated along the same lines as the evaluation of the double integral itself (11).

Similar considerations also yield the different derivatives of the exponential mapping as involved in the discretized weak form (9)

$$\begin{aligned} \frac{\partial}{\partial \xi} \Big|_{\xi=0} \exp(\Psi^h + \xi \delta\Psi^h) &= \sum_{i,j=1}^d \left(\frac{e^{\lambda_i}}{\lambda_i - \lambda_j} + \frac{e^{\lambda_j}}{\lambda_j - \lambda_i} \right) \mathbf{P}_i \delta\Psi^h \mathbf{P}_j \\ &= \sum_{i,j=1}^d e^{\lambda_i/2} e^{\lambda_j/2} \frac{\sinh((\lambda_i - \lambda_j)/2)}{(\lambda_i - \lambda_j)/2} \mathbf{P}_i \delta\Psi^h \mathbf{P}_j \\ \nabla \cdot \exp(\Psi^h) &= \sum_{i,j,k=1}^d e^{\lambda_j/2} e^{\lambda_k/2} \frac{\sinh((\lambda_j - \lambda_k)/2)}{(\lambda_j - \lambda_k)/2} \mathbf{P}_j \partial_i \Psi^h \mathbf{P}_k \mathbf{e}_i. \end{aligned}$$

Here, the vectors \mathbf{e}_i denote the Cartesian basis vectors. Additionally, due to the GLS stabilization, the variational derivative has to be considered for $\nabla \cdot \exp(\Psi^h)$. The analysis yields

$$\begin{aligned} \frac{\partial}{\partial \xi} \Big|_{\xi=0} \nabla \cdot \exp(\Psi^h + \xi \delta\Psi^h) &= \sum_{i,j,k=1}^d e^{\lambda_j/2} e^{\lambda_k/2} \frac{\sinh((\lambda_j - \lambda_k)/2)}{(\lambda_j - \lambda_k)/2} \mathbf{P}_j \partial_i \delta\Psi^h \mathbf{P}_k \mathbf{e}_i \\ &+ \sum_{i,j,k=1}^d \left(\frac{e^{\lambda_i}}{(\lambda_i - \lambda_j)(\lambda_i - \lambda_k)} + \frac{e^{\lambda_j}}{(\lambda_j - \lambda_i)(\lambda_j - \lambda_k)} + \frac{e^{\lambda_k}}{(\lambda_k - \lambda_i)(\lambda_k - \lambda_j)} \right) \\ &\quad \cdot \sum_{l=1}^d [\mathbf{P}_i \delta\Psi^h \mathbf{P}_j \partial_l \Psi^h \mathbf{P}_k \mathbf{e}_l + \mathbf{P}_k \partial_l \Psi^h \mathbf{P}_j \delta\Psi^h \mathbf{P}_i \mathbf{e}_l]. \end{aligned}$$

For the numerical implementation, we will have to further rewrite the factor in the second sum, as it is in this form not appropriate for evaluation in the proximity of degenerate eigenvalues. Introducing auxiliary

variables $x = (\lambda_i - \lambda_j)/3$, $y = (\lambda_i - \lambda_k)/3$, and $z = (\lambda_j - \lambda_k)/3$, it can be reformulated as

$$\begin{aligned} & \frac{e^{\lambda_i}}{(\lambda_i - \lambda_j)(\lambda_i - \lambda_k)} + \frac{e^{\lambda_j}}{(\lambda_j - \lambda_i)(\lambda_j - \lambda_k)} + \frac{e^{\lambda_k}}{(\lambda_k - \lambda_i)(\lambda_k - \lambda_j)} \\ &= \frac{1}{9} e^{\lambda_i/3} e^{\lambda_j/3} e^{\lambda_k/3} \left[\frac{e^x - 1}{x} \frac{e^y - 1}{y} + \frac{e^{-x} - 1}{-x} \frac{e^z - 1}{z} + \frac{e^{-y} - 1}{-y} \frac{e^{-z} - 1}{-z} \right. \\ & \quad \left. + \frac{1}{y - x} \left(\frac{e^{-x} - 1}{-x} - \frac{e^{-y} - 1}{-y} \right) + \frac{1}{x + z} \left(\frac{e^x - 1}{x} - \frac{e^{-z} - 1}{-z} \right) + \frac{1}{y - z} \left(\frac{e^y - 1}{y} - \frac{e^{-z} - 1}{z} \right) \right]. \end{aligned} \quad (13)$$

Thus, the evaluation is once again reduced to difference quotients. The latter, which already appeared in Eq. (12), can be easily approximated by a Taylor series in the vicinity of vanishing denominators

$$\frac{g(x) - g(y)}{x - y} = g^{(1)}\left(\frac{x + y}{2}\right) + \frac{(x - y)^2}{24} g^{(3)}\left(\frac{x + y}{2}\right) + \mathcal{O}((x - y)^4).$$

Here $g(x)$ can stand either for $f(x)$ as in the case of Eq. (12) or for $(e^x - 1)/x$ as in Eq. (13). In the former case the Taylor series is used for $|x - y| < 10^{-2}$ and in the latter case for $|x - y| < 10^{-3}$ in order to account for the use of floating point arithmetic with double precision. In addition, the derivatives of $g(x)$ also have to be approximated for small values of x , which for $f(x)$ is performed beneath $|x| < 10^{-1}$ and for $(e^x - 1)/x$ below $|x| < 10^{-3}$. The numbers were obtained by comparing results of a naive double precision implementation with the results computed in a much higher precision [24], and afterwards choosing the Taylor polynomials such that the relative error should not exceed $\sim 10^{-10}$. A higher precision is also quite unlikely to be needed as both terms enter the linear equation system only on the left-hand side, such that they only influence the convergence, but not the accuracy of the solution. As we will later see, the convergence is influenced even more by the inexact solution of the equation system through iterative linear solvers.

It should be noted that such a special treatment for the other functions involved is in general unnecessary. The hyperbolic functions $\tanh(x/2)$ and $\sinh(x/2)$ can be readily used if $x/2 \neq 0$, assuming their implementation is correctly rounded close to 0 and the rounding mode is set to round to nearest [25]. For $(e^x - 1)/x$, the accuracy near $x \approx 0$ can be greatly improved by using a trick [26] and evaluating

$$\frac{e^x - 1}{x} = \frac{y - 1}{\log y} \quad \text{with } y = e^x,$$

which is substituted by 1 in the case of $y = 1$.

All other terms on the left-hand side of the linear equation system arising from (9) can be derived as usual. The derivatives originating from the stabilization terms, in particular the derivatives of $\tau_{cons}(\mathbf{u}^h \cdot \nabla) \Phi^h$ with respect to \mathbf{u}^h , are typically omitted, as they decrease the robustness of the Newton–Raphson algorithm. Nonetheless, they are an essential ingredient for quadratic convergence, which will also be discussed in the next section.

In our implementation we use an ILUT-preconditioned FGMRES implementation to solve the resulting linear systems (cf. [27, 28]).

4. Benchmarks

In this section we will use the newly derived method to study two benchmarks: the sedimenting sphere benchmark and a variation thereof with the sphere replaced by a tri-axial ellipsoid.

4.1. Sedimenting sphere

The sedimenting sphere in a tube benchmark is, in addition to the drag on confined cylinder benchmark, one of the classic benchmarks that has been used in the past to measure the performance of numerical codes and different constitutive models. It has been intensively studied experimentally, as well as numerically,

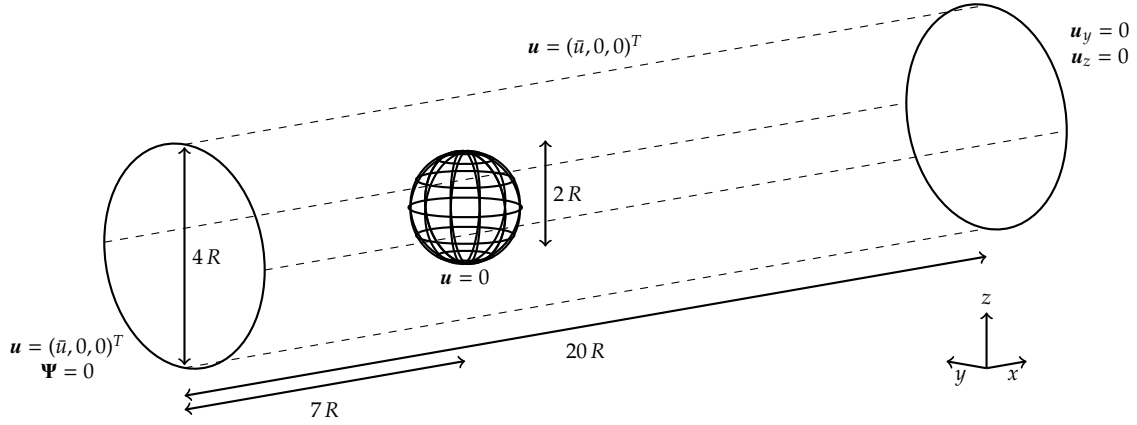


Figure 2: Illustration of the geometry and prescribed boundary conditions for the simulation of a uniform flow past a static sphere of radius R .

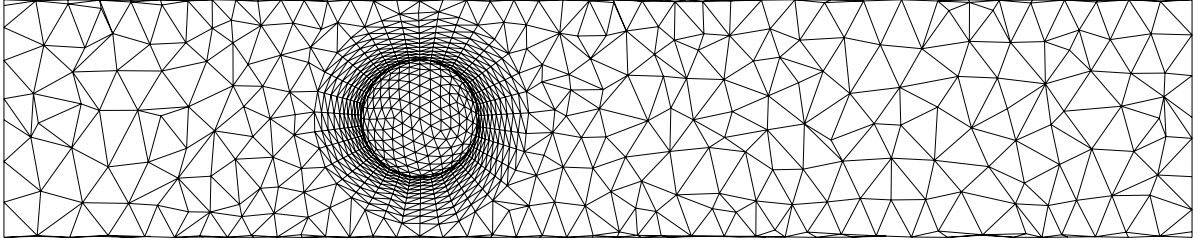


Figure 3: Cut through the xy -plane of Mesh M1.

where numerous results for the upper-convected Maxwell model were obtained. For a thorough review of the two aspects we refer to [29, 3] and the references therein. Our analysis will be mostly centered around the Oldroyd-B model, which was already analyzed in [30, 31, 32, 33], as well as the Giesekus model. In contrast to the just-mentioned literature, we will not exploit the rotational symmetry in order to perform an in essence two-dimensional simulation of the three-dimensional problem, but will solve the problem in three dimensions. The latter, although computationally more expensive, is of course more flexible and preferred with the view on future applications. As is commonly done, we will furthermore restrict ourselves to the simulation of the fully-developed flow condition, where the sphere is sedimenting at constant speed, such that through a shift into the reference frame of the sphere, we can reformulate the problem as a stationary problem of a sphere at rest within a flow with uniform velocity \bar{u} . Moreover, the gravitational force is neglected; with the exception of a missing buoyancy term in the pressure p , this will not lead to any change of the flow field.

The geometry, as illustrated in Fig. 2, features a sphere of radius R . The sphere is located in the center of a tube with radius $2R$ and is exposed to a uniform stream $\mathbf{u} = (\bar{u}, 0, 0)^T$. Based on the geometry, the flow conditions, and the relaxation time λ , we define the Weissenberg number as

$$Wi = \frac{\lambda \bar{u}}{R}.$$

It should be mentioned that the choice of the flow in x -direction is solely for the purpose of a better illustration. The boundary conditions, as shown in Fig. 2, are a no-slip condition on the sphere, a uniform stream of stress-free polymers ($\Psi = 0$) at the inflow, and vanishing velocities perpendicular to the symmetry axis on the outflow. In accordance with the literature, only the creeping flow limit ($Re = 0$) is considered and the

	M1	M2	M3
Number of elements on the sphere	676	2602	9432
Total number of nodes	42788	217789	970454
Total number of elements	29791	157757	714417
Krylov-space dimension	150	300 / 350	400
ILUT maximal fill-in n_{ILUT}	120 / 200	120 / 200 / 250	120 / 200 / 250
ILUT threshold	10^{-4}	10^{-4}	10^{-4}
Number of cores	32	256 / 512	2048

Table 1: Mesh properties and solver parameters for the sedimenting sphere benchmark.

Wi	K						
	M1	M2	M3	[30]	[31]	[32]	[33]
0.1	5.90022	5.90472	5.90576				
0.2	5.80240	5.80646	5.80763				
0.3	5.68858	5.69227	5.69356	5.69368	5.6963		
0.4	5.58068	5.58390	5.58527				
0.5	5.48692	5.48953	5.49093			5.4852	
0.6	5.40899	5.41086	5.41227	5.41225	5.4117	5.4009	
0.7	5.34592	5.34700	5.34838			5.3411	
0.8	5.29582	5.29616	5.29747			5.2945	
0.9	5.25660	5.25639	5.25761	5.25717		5.2518	
1.0	5.22628	5.22586	5.22700			5.2240	
1.1	5.20312	5.20292	5.20402			5.2029	
1.2	5.18568	5.18619	5.18733	5.18648		5.1842	5.1877
1.3	5.17278	5.17449	5.17581				5.1763
1.4	5.16354	5.16689	5.16851				
1.5	5.15723	5.16261		5.15293			

Table 2: Results for the correction factor K of the drag on the sphere when using the Oldroyd-B model.

viscosity ratio is, in all conducted simulations, chosen as $\beta = \mu_s/\mu = 0.5$.

As already indicated in the previous section, a tetrahedral \mathbb{P}_2 mesh was used to discretize the domain. A cut through the coarsest of the used meshes can be seen in Fig. 3. All meshes feature a $0.9R$ -thick boundary layer around the sphere in order to properly resolve steep gradients. Further mesh properties as well as the linear solver parameters can be taken from Tab. 1. Moreover, during the calculations the Weissenberg number was consecutively increased in such a way that the last result always served as an initial guess for the following run. Run times for a single simulation range approximately from 400 s to 700 s wall-clock time for the Meshes M1 and M2 on the Intel-based RWTH cluster. For the finest mesh, the IBM-based Juqueen computer was used, resulting in run times of 1300 – 2200 s.

4.1.1. Oldroyd-B model

The use of the described benchmark in conjunction with the Oldroyd-B model has been covered extensively in literature. One widely recognized performance quantity is the wall correction factor K , which is given as the ratio of the drag force on the sphere to the Stokesian drag of a sphere in an unbounded Newtonian fluid

$$K = \frac{1}{6\pi\mu R\bar{u}} \int_{\Gamma_{\text{Sphere}}} \mathbf{e}_x^T \left[-p\mathbf{1} + 2\mu_s\boldsymbol{\varepsilon}(\mathbf{u}) + \frac{\mu_p}{\lambda} (e^{\boldsymbol{\Psi}} - \mathbf{1}) \right] \mathbf{n}. \quad (14)$$

Here, \mathbf{n} denotes the unit normal field on the sphere, as usual.

The results of the simulations as presented in Tab. 2 match the results in literature quite well: Generally convergence can — independent of mesh size — be claimed up to a Weissenberg number of $Wi = 1.4$. Above this threshold, the conditioning of the linearized system regresses. This can be mitigated only to a certain extent by an increased number of GMRES iterations and an increased ILUT fill-in, but otherwise usually

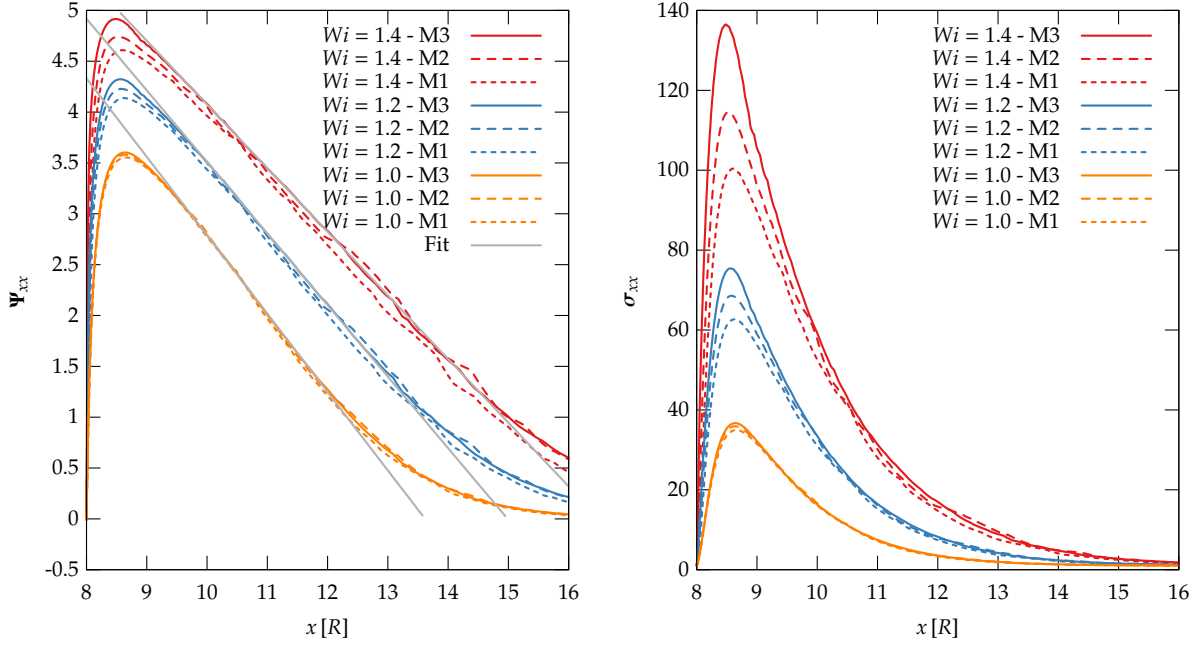


Figure 4: Ψ_{xx} and σ_{xx} plotted along the centerline in the wake of the sphere.

leads to a failure of the simulation.

It should be noted that the drag might not necessarily be the best benchmark quantity to measure the performance of numerical discretizations, which may yield perfect drag results while not being able to properly predict other important flow characteristics. One of these characteristics is the extensional flow in the wake of the sphere, where the polymers are stretched along the flow direction. This is of special importance for the Oldroyd-B model, which, as it corresponds to the microscopic Hookean-dumbbell model, has the property that the solution blows up in a purely extensional flow if the extensional rate exceeds a critical point — simply put, the dumbbells become infinitely long. Although there has not been a conclusive proof in literature yet, it is believed that a similar mechanism is also responsible for the limitation in the Weissenberg number for the feasible simulations in the falling sphere benchmark. To highlight this similarity, notice that symmetry dictates Ψ and $\nabla \mathbf{u}$ to be diagonal along the centerline, such that the constitutive equation of Ψ_{xx} in Eq. (3) reduces to

$$\mathbf{u}_x \partial_x \Psi_{xx} - 2 \partial_x \mathbf{u}_x = -\frac{1}{\lambda} (1 - e^{-\Psi_{xx}}). \quad (15)$$

Considering that at any extremal point x^* of Ψ_{xx} the derivative has to vanish, rearranging this equation yields

$$\Psi_{xx}(x^*) = -\log(1 - 2\lambda \partial_x \mathbf{u}_x(x^*)).$$

Thus, with $\partial_x \mathbf{u}_x(x^*)$ approaching $1/(2\lambda)$ the component Ψ_{xx} blows up. Of course, nothing particular on the behavior of $\partial_x \mathbf{u}_x$ can be inferred within the framework of one-dimensional analysis due to the incompressibility constraint.

The Ψ_{xx} actually predicted by the simulation can be seen in Fig. 4. One of the points that becomes directly apparent is that in these simulations mesh convergence can only be claimed up to Weissenberg numbers $Wi = 1.0 - 1.2$. Above these values, it seems that despite a boundary-layer-resolving mesh, the fluid characteristics in that region still cannot be accurately described. This effect becomes even more pronounced looking at σ_{xx} , which modulo numerical noise is given by $\sigma_{xx} = \exp \Psi_{xx}$ and is also depicted in Fig. 4. There, of course, a slight deviation of an already large Ψ_{xx} is further amplified by the exponential

Wi	K								
	$\alpha = 0.001$			$\alpha = 0.01$			$\alpha = 0.1$		
	M1	M2	M3	M1	M2	M3	M1	M2	M3
0.1	5.89918	5.90369	5.90473	5.88997	5.89464	5.89573	5.81454	5.82032	5.82166
0.2	5.79863	5.80274	5.80393	5.76691	5.77147	5.77275	5.56351	5.57002	5.57160
0.3	5.68098	5.68479	5.68610	5.62095	5.62552	5.62694	5.31523	5.32188	5.32349
0.4	5.56845	5.57185	5.57324	5.47847	5.48300	5.48451	5.09969	5.10625	5.10785
0.5	5.46934	5.47222	5.47366	5.34928	5.35374	5.35531	4.91688	4.92331	4.92489
0.6	5.38538	5.38763	5.38910	5.23534	5.23965	5.24127	4.76150	4.76781	4.76938
0.7	5.31561	5.31714	5.31861	5.13538	5.13952	5.14118	4.62842	4.63461	4.63616
0.8	5.25811	5.25891	5.26037	5.04716	5.05109	5.05280	4.51345	4.51955	4.52109
0.9	5.21075	5.21091	5.21235	4.96839	4.97211	4.97387	4.41335	4.41936	4.42090
1.0	5.17150	5.17122	5.17264	4.89714	4.90066	4.90248	4.32556	4.33150	4.33303
1.1	5.13857	5.13811	5.13955	4.83192	4.83528	4.83716	4.24805	4.25394	4.25545
1.2	5.11050	5.11012	5.11165	4.77169	4.77491	4.77684	4.17920	4.18503	4.18653
1.3	5.08611	5.08608	5.08774	4.71569	4.71879	4.72077	4.11769	4.12347	4.12496
1.4	5.06448	5.06501	5.06688	4.66336	4.66637	4.66840	4.06245	4.06818	4.06966
1.5	5.04489	5.04617	5.04829	4.61432	4.61725	4.61931	4.01260	4.01828	4.01975
1.6		5.02897	5.03139	4.56825	4.57111	4.57319	3.96740	3.97303	3.97448
1.8				4.48402	4.48676	4.48886	3.88863	3.89413	3.89557
2.0				4.40900	4.41166	4.41375	3.82234	3.82771	3.82914
2.2				4.34189	4.34447	4.34653	3.76580	3.77103	3.77245
2.4				4.28156	4.28409	4.28612	3.71703	3.72211	3.72352
2.6				4.22709	4.22960	4.23159	3.67452	3.67943	3.68085
3.0				4.13269	4.13526	4.13716	3.60400	3.60857	3.61001
3.5				4.03595	4.03881	4.04057	3.53552	3.53969	3.54117
4.0				3.95673	3.96008	3.96170	3.48206	3.48589	3.48740
4.5				3.89055	3.89454	3.89602	3.43910	3.44264	3.44418
5.0				3.83433	3.83905	3.84040	3.40376	3.40707	3.40864
5.5				3.78591	3.79140	3.79265	3.37414	3.37728	3.37886
6.5				3.70655	3.71357	3.71469	3.32716	3.33010	3.33166
7.5				3.64403	3.65246	3.65355	3.29144	3.29432	3.29584
8.0				3.61743	3.62651	3.62762	3.27658	3.27947	3.28096
8.5				3.59334	3.60301	3.60415	3.26328	3.26619	3.26765
9.0				3.57140	3.58160	3.58280	3.25130	3.25424	3.25567
9.5				3.55134	3.56202	3.56328	3.24044	3.24344	3.24482
10.0				3.53290	3.54402	3.54535	3.23055	3.23360	3.23495
11.0				3.50015		3.51352	3.21318	3.21637	3.21764
12.0				3.47192		3.48607	3.19839	3.20173	3.20293
13.0				3.44729		3.46211	3.18564	3.18914	3.19027
14.0				3.42558		3.44098	3.17452	3.17816	3.17923
15.0				3.40628		3.42218	3.16472	3.16851	3.16952

Table 3: Results for the correction factor K of the drag on the sphere when using the Giesekus model.

function. Furthermore, it should also be noted that the point where Ψ_{xx} attains its maximum seems to reach its maximal x -value at $Wi = 0.8$. For higher Weissenberg numbers the maximum is then shifted again in the direction of the sphere.

Considering these peculiarities and the general non-linearity of the governing equations, it is even more remarkable that on the downward slope of Ψ_{xx} in Fig. 4 the field shows a linear behavior. Performing a least squares fit of linear curves to the simulated data in the region $x = 10R - 12R$ on Mesh M3 yields slopes of $m = -0.6259 R^{-1}$ for $Wi = 1.4$, $m = -0.7037 R^{-1}$ for $Wi = 1.2$, and $m = -0.7708 R^{-1}$ for $Wi = 1.0$. The resulting linear curves can be examined in Fig. 4. It is yet unclear which mechanism leads to this linear behavior.

4.1.2. Giesekus model

A similar analysis as for the Oldroyd-B model is also conducted for the Giesekus model that extends the Oldroyd-B model by an additional term. In fact, the Oldroyd-B model is a special case of the Giesekus model for a vanishing mobility parameter $\alpha = 0$.

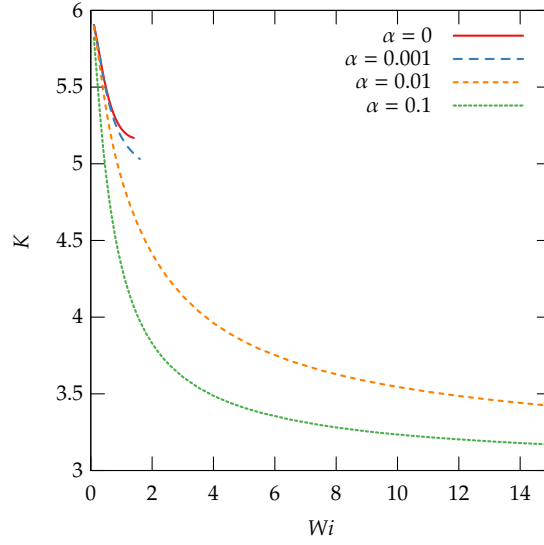


Figure 5: Wall correction factor K plotted for different values of the mobility α , computed on the Mesh M3.

As before, the quantity studied first is the drag correction factor K for several Weissenberg numbers Wi and varying mobility α . The results are collected in Tab. 3 and depicted in Fig. 5. It is notable that, for the smallest $\alpha = 0.001$, the model exhibits similar numerical behavior as the Oldroyd-B model, namely convergent results only up to $Wi = 1.6$. This is to be expected, higher Weissenberg numbers may be achievable with finer meshes in contrast to the Oldroyd-B model. Increasing α shows that the drag on the sphere decreases in general, which is attributable to the shear-thinning properties of a Giesekus fluid. Moreover, for all performed numerical calculations the drag is monotonically decreasing with increasing Weissenberg number Wi , and there are indications that K reaches a plateau for sufficiently high Wi .

Looking at the extensional flow characteristics of the Giesekus model in the wake of the sphere, it already

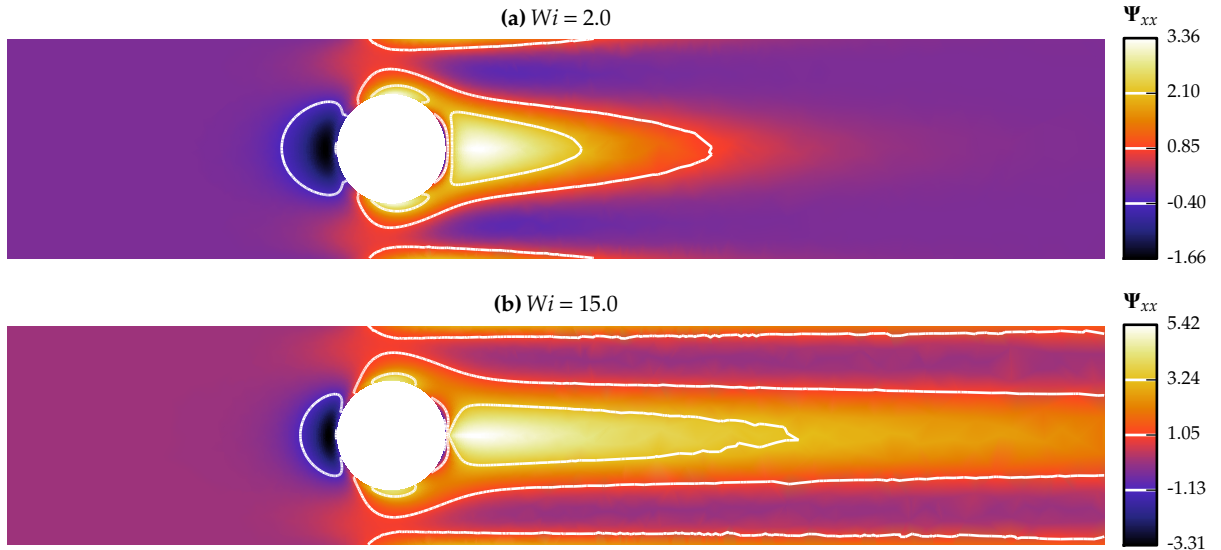


Figure 6: Cut through the xy -plane of Mesh M3, illustrating Ψ_{xx} for different Weissenberg numbers and $\alpha = 0.1$.

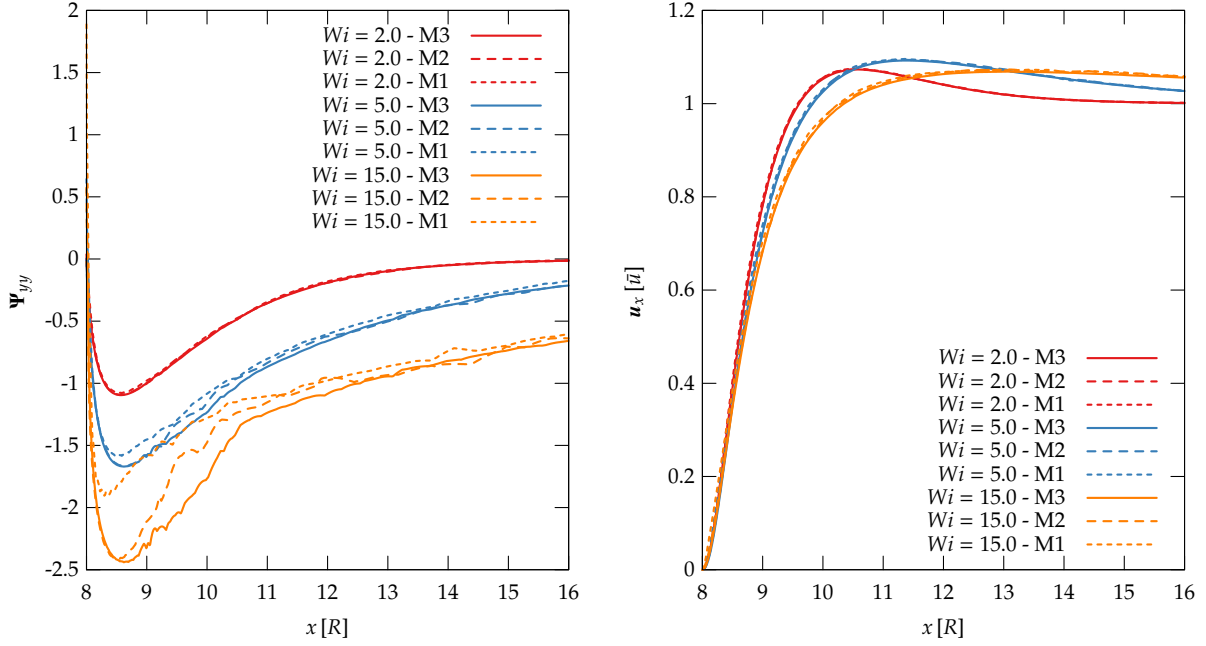


Figure 7: Ψ_{yy} and u_x plotted along the centerline in the wake of the sphere for $\alpha = 0.1$.

becomes apparent from the equivalent of Eq. (15) that the model is better-behaved:

$$u_x \partial_x \Psi_{xx} - 2 \partial_x u_x = -\frac{1}{\lambda} (1 - 2\alpha - (1 - \alpha)e^{-\Psi_{xx}} + \alpha e^{\Psi_{xx}}).$$

Here, the additional $\alpha \exp(\Psi_{xx})$ term can potentially compensate an increase of $\partial_x u_x$ exceeding $1/(2\lambda)$, thus limiting the increase of Ψ_{xx} . The resulting computations of Ψ_{xx} for two different Weissenberg numbers $Wi = 2.0$ and $Wi = 15.0$ are shown in Fig. 6. The results reflect clearly that with increasing Weissenberg number, the polymers need more time to relax to their stress-free state, which means that they are transported further downstream before they reach this state. As such, the Ψ_{xx} contours also extend further downstream for higher Weissenberg numbers than for lower ones. As a consequence the demands on the used geometry and meshes increase: They need to sustain a high refinement level over a larger region in the wake of the sphere.

This effect becomes even more noticeable when considering the other degrees of freedom in our simulation. In Fig. 7, Ψ_{yy} has been plotted along the centerline for different Weissenberg numbers. The first point to notice is that mesh convergence can be reached within the boundary-layer-adjusted mesh around the sphere, but as soon as the mesh resolution decreases, the accuracy in the to-be-predicted degree of freedom Ψ_{yy} is lost. The impact becomes more severe the higher the Weissenberg number is. In addition, by inspecting Fig. 7, it seems that for $Wi = 15.0$, Ψ_{yy} exhibits a small kink around $x = 10.5 R$ on Mesh M3, which may be attributable to a still insufficient refinement level of the mesh in that particular region.

On the other hand, the fact that Ψ_{yy} is negative also means that errors therein are exponentially damped in $\sigma_{yy} = \exp \Psi_{yy}$. Since the latter is what essentially contributes to the momentum equation, it is not much of a surprise that the velocity component depicted in Fig. 7 is still smooth for all used meshes. Furthermore, velocity overshoots exceeding \bar{u} are clearly visible, in contrast to Oldroyd-B simulations. Moreover, the downstream relaxation is once more delayed with increasing Weissenberg number.

4.1.3. Performance of the Newton–Raphson algorithm

It is important to note that the Newton–Raphson method indeed delivers quadratic convergence up to the point where the errors emerging from the inexact linear solution or the limited floating-point accuracy

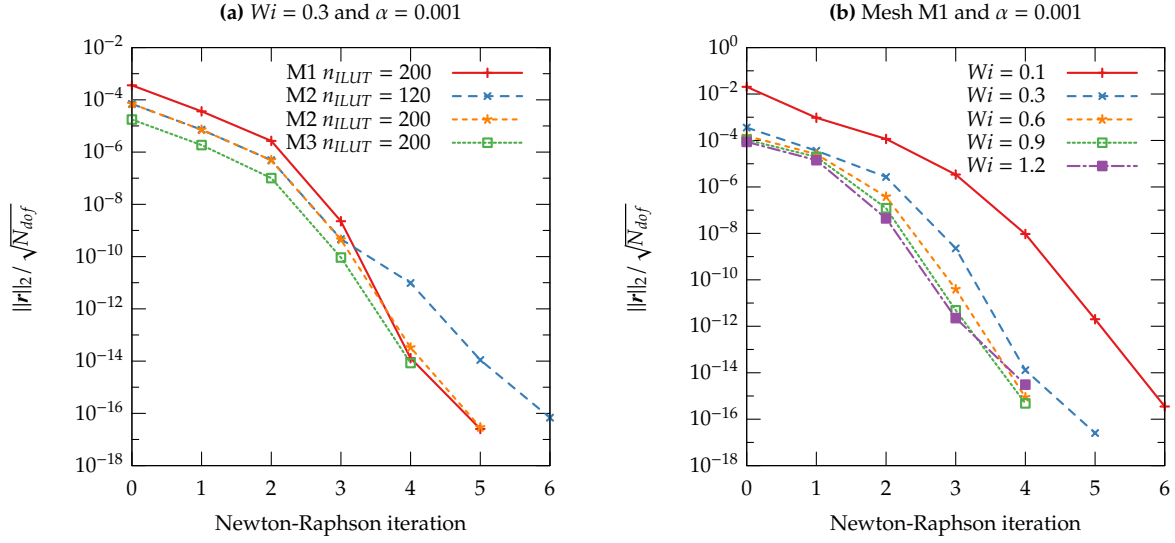


Figure 8: Convergence behavior of the Newton-Raphson algorithm for different settings.

become dominant. Fig. 8 depicts a comparative study of the residual after each Newton-Raphson iteration across different meshes, as well as an analysis of the convergence behavior for different Weissenberg numbers. In both cases, the residual has been evaluated in the Euclidean norm and scaled by the square root of the total number of degrees of freedom in order to make the results comparable across different mesh sizes. As one sees in Fig. 8a, the convergence history can be roughly split into three phases: In the first step, the improvement is rather moderate; at most linear convergence was obtained. In the second phase, e.g., for the Mesh M3, one observes a relative improvement of the residual by a factor of 18.34 in the second step and an improvement by a factor of $1097 > (18.34)^2$ in the third step; thus slightly exceeding quadratic convergence. It becomes apparent from Fig. 8a that this convergence is mesh-independent. The third phase is then dominated by errors introduced by the inexact solution of the linear equation systems. This can be deduced from the results in Fig. 8a, where the calculations on Mesh M2 were performed using two different ILUT fill-in settings. A reduction of the ILUT fill-in, and a therewith increased error in the solution of the linear systems, directly leads to a deterioration of the quadratic convergence to at most asymptotically linear convergence [34]. Furthermore, in the last steps the convergence is limited by the fact that a residual far beneath 10^{-16} is in general not attainable due to the floating-point arithmetic used.

In Fig. 8b, one notices that, using the result obtained for the previously calculated Weissenberg number as an initial guess for the subsequent calculation, the convergence progression is similar across the consecutive runs. Only the starting point $Wi = 0.1$ does not fully fit into this picture, which on the one hand has to be attributed to the circumstance that for this case the initial guess was set to zero in the interior of the computational domain, and on the other hand is a consequence of the derivative of $\tau_{cons}(\mathbf{u}^h \cdot \nabla)\Phi^h$ in the discretized weak form being neglected (cf. Section 3.2). The latter is a remedy for the fact that without these additional terms, the iterative scheme seems to be more robust with regard to the choice of the initial guess.

4.2. Sedimenting ellipsoid

In order to demonstrate the applicability of the proposed method to a truly three-dimensional problem, a case similar to the sedimenting sphere benchmark is considered, but with the sphere replaced by a tri-axial ellipsoid. The latter was chosen with the semi-principal axes aligned to the coordinate axes. The length of the axes in x, y , and z direction were set to $a = 1.25R$, $b = 1.0R$, and $c = 0.8R$, respectively, such that in accordance with the findings in [35], the semi-major axis coincides with the main flow direction for $Re = 0$. The tube radius was kept as $2R$.

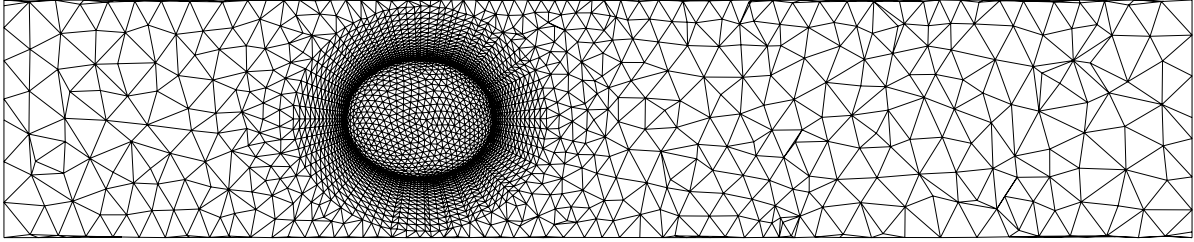


Figure 9: Cut through the xy -plane of Mesh M4, as used in the calculations with an ellipsoid.

	M4
Number of elements on the ellipsoid	2706
Total number of nodes	218663
Total number of elements	158353
Krylov-space dimension	300
ILUT maximal fill-in n_{ILUT}	200
ILUT threshold	10^{-4}
Number of cores	256

Table 4: Mesh and solver attributes used for the sedimenting ellipsoid benchmark.

The mesh, as depicted in Fig. 9, was chosen similar to the Mesh M2 in the sedimenting sphere benchmark, which already provided a good trade-off between computational cost and accuracy in the drag computation. Therefore, the GMRES/ILUT parameters were also chosen accordingly, as can be seen in Tab.4.

Our main objective of the investigation was the drag correction factor K , where the latter has been defined for the sake of simplicity as in the case of the falling sphere, cf. Eq. (14). Nonetheless, the Stokesian drag formula can be generalized to ellipsoids in principle [36]. The results in Tab. 5 confirm the general trend of the simulations with the spherical geometry: The drag decreases monotonically with increasing Weissenberg number. It can also be stated that the general drag level is below the drag levels obtained in the simulations with a sphere as obstacle, which may be attributed to the reduced cross section. With increasing α , higher Weissenberg numbers can be attained, and the effect of reduced drag due to increased shear-thinning becomes visible.

5. Conclusion and discussion

The main objective of this paper was to derive a log-conformation formulation that on the one hand inherits the stability properties of the originally proposed log-conformation formulation [8], but on the other hand also paves the way for an application of Newton’s method in numerical simulations. Furthermore, we especially sought a description that could be applied in three dimensions with the same ease as the previously published two-dimensional approaches [13, 14].

To demonstrate the numerical benefit of this approach, we implemented a proof-of-concept three-dimensional finite element solver and subsequently tested it by means of the sedimenting sphere and ellipsoid benchmarks. The simulations exhibited the best-possible convergence properties of quadratic-convergence.

Since the new constitutive equations are just a rewording of the original log-conformation equations, the proposed formulation cannot further improve the stability. As such, we were not able to obtain results beyond a Weissenberg number of $Wi = 1.4$ for a sphere sedimenting through an Oldroyd-B fluid. Since switching to the Giesekus model removed this limitation, the characteristic behavior of the Oldroyd-B fluid in extensional flow regimes might be the underlying reason for this restriction.

In addition to the just-mentioned advantages for the numerical application, our formulation is intrinsically defined in an undiscretized setting, which may reveal new perspectives on the analytical properties of the

Wi	K			
	$\alpha = 0$	$\alpha = 0.001$	$\alpha = 0.01$	$\alpha = 0.1$
0.1	4.90847	4.90782	4.90211	4.85331
0.2	4.85959	4.85715	4.83621	4.68884
0.3	4.79819	4.79305	4.75092	4.50990
0.4	4.73648	4.72791	4.66130	4.34532
0.5	4.68082	4.66810	4.57513	4.20056
0.6	4.63365	4.61608	4.49540	4.07438
0.7	4.59537	4.57217	4.42252	3.96425
0.8	4.56535	4.53566	4.35581	3.86772
0.9	4.54252	4.50538	4.29432	3.78269
1.0	4.52568	4.48007	4.23718	3.70739
1.1	4.51370	4.45854	4.18372	3.64038
1.2	4.50554	4.43976	4.13345	3.58045
1.3	4.50034	4.42286	4.08604	3.52658
1.4	4.49738	4.40717	4.04124	3.47795
1.5		4.39215	3.99883	3.43385
1.6		4.37747	3.95867	3.39369
1.8			3.88450	3.32332
2.0			3.81772	3.26370
\vdots			\vdots	\vdots
10.0			3.01520	2.71617
11.0			2.98506	2.69985
12.0			2.95902	2.68597
13.0			2.93626	2.67400
14.0			2.91617	2.66356
15.0			2.89827	2.65437

Table 5: Results for the correction factor K of the drag on the ellipsoid.

used constitutive models in the future. In particular, the seamless incorporation of the so-called free-energy estimates in the log-conformation formulation [37] and their application to the global-in-time existence of solutions [38, 39] may give new insights.

6. Acknowledgments

The author gratefully acknowledges support from the German Research Foundation (DFG) grant “Computation of Die Swell Behind a Complex Profile Extrusion Die Using a Stabilized Finite Element Method for Various Thermoplastic Polymers” and the DFG program GSC 111 (AICES Graduate School). The computations were conducted on computing clusters provided by the Jülich Aachen Research Alliance (JARA). Furthermore, I want to thank Marek Behr, Stefanie Elgeti, and Stefan Haßler for their indispensable remarks during the preparation of the manuscript.

References

- [1] A. L. Marsden, Y. Bazilevs, C. C. Long, M. Behr, Recent advances in computational methodology for simulation of mechanical circulatory assist devices, *Wiley Interdisciplinary Reviews: Systems Biology and Medicine* 6 (2) (2014) 169–188.
- [2] L. Pauli, M. Behr, S. Elgeti, Towards shape optimization of profile extrusion dies with respect to homogeneous die swell, *Journal of Non-Newtonian Fluid Mechanics* 200 (2013) 79–87. doi : 10.1016/j.jnnfm.2012.12.002.
- [3] R. G. Owens, T. N. Phillips, *Computational Rheology*, 2nd Edition, Imperial College Press, 2005.
- [4] M. Griebel, A. Rüttgers, Multiscale simulations of three-dimensional viscoelastic flows in a square–square contraction, *Journal of Non-Newtonian Fluid Mechanics* 205 (2014) 41 – 63. doi : 10.1016/j.jnnfm.2014.01.004.
- [5] J. G. Oldroyd, On the formulation of rheological equations of state, *Proceedings of the Royal Society of London. Series A. Mathematical and Physical Sciences* 200 (1063) (1950) 523–541.
- [6] H. Giesekus, A simple constitutive equation for polymer fluids based on the concept of deformation-dependent tensorial mobility, *Journal of Non-Newtonian Fluid Mechanics* 11 (1) (1982) 69–109.
- [7] R. Keunings, On the high Weissenberg number problem, *Journal of Non-Newtonian Fluid Mechanics* 20 (1986) 209–226.

- [8] R. Fattal, R. Kupferman, Constitutive laws for the matrix-logarithm of the conformation tensor, *Journal of Non-Newtonian Fluid Mechanics* 123 (2) (2004) 281–285.
- [9] M. A. Hulsen, A sufficient condition for a positive definite configuration tensor in differential models, *Journal of Non-Newtonian Fluid Mechanics* 38 (1) (1990) 93–100.
- [10] O. M. Coronado, D. Arora, M. Behr, M. Pasquali, A simple method for simulating general viscoelastic fluid flows with an alternate log-conformation formulation, *Journal of Non-Newtonian Fluid Mechanics* 147 (3) (2007) 189–199.
- [11] H. Damanik, J. Hron, A. Ouazzani, S. Turek, A monolithic FEM approach for the log-conformation reformulation (LCR) of viscoelastic flow problems, *Journal of Non-Newtonian Fluid Mechanics* 165 (19) (2010) 1105–1113.
- [12] Y. Kwon, Finite element analysis of planar 4:1 contraction flow with the tensor-logarithmic formulation of differential constitutive equations, *Korea-Australia Rheology Journal* 16 (4) (2004) 183–191.
- [13] P. Knechtges, M. Behr, S. Elgeti, Fully-implicit log-conformation formulation of constitutive laws, *Journal of Non-Newtonian Fluid Mechanics* 214 (2014) 78–87. [arXiv:1406.6988](https://arxiv.org/abs/1406.6988), doi:10.1016/j.jnnfm.2014.09.018.
- [14] P. Saramito, On a modified non-singular log-conformation formulation for Johnson–Segalman viscoelastic fluids, *Journal of Non-Newtonian Fluid Mechanics* 211 (2014) 16–30. doi:10.1016/j.jnnfm.2014.06.008.
- [15] R. Adams, J. Fournier, *Sobolev Spaces*, 2nd Edition, Vol. 140 of *Pure and Applied Mathematics*, Academic Press, 2003.
- [16] W. Rudin, *Functional Analysis*, McGraw-Hill, New York, 1991.
- [17] K. Yosida, *Functional Analysis*, Springer-Verlag, 1980.
- [18] R. M. Wilcox, Exponential Operators and Parameter Differentiation in Quantum Physics, *Journal of Mathematical Physics* 8 (4) (1967) 962–982.
- [19] A. N. Brooks, T. J. R. Hughes, Streamline upwind/Petrov-Galerkin formulations for convection dominated flows with particular emphasis on the incompressible Navier-Stokes equations, *Computer Methods in Applied Mechanics and Engineering* 32 (1) (1982) 199–259.
- [20] L. P. Franca, S. L. Frey, T. J. R. Hughes, Stabilized finite element methods: I. Application to the advective-diffusive model, *Computer Methods in Applied Mechanics and Engineering* 95 (2) (1992) 253–276.
- [21] L. P. Franca, S. L. Frey, Stabilized finite element methods: II. The incompressible Navier-Stokes equations, *Computer Methods in Applied Mechanics and Engineering* 99 (2) (1992) 209–233.
- [22] M. A. Behr, L. P. Franca, T. E. Tezduyar, Stabilized finite element methods for the velocity-pressure-stress formulation of incompressible flows, *Computer Methods in Applied Mechanics and Engineering* 104 (1) (1993) 31–48.
- [23] T. Kato, *Perturbation Theory for Linear Operators*, Springer-Verlag, 1995.
- [24] F. Johansson, et al., `mpmath`: a Python library for arbitrary-precision floating-point arithmetic (June 2014). URL <http://mpmath.org>
- [25] J.-M. Muller, N. Brisebarre, F. De Dinechin, C.-P. Jeannerod, V. Lefevre, G. Melquiond, N. Revol, D. Stehlé, S. Torres, *Handbook of Floating-Point Arithmetic*, Springer-Verlag, 2010.
- [26] N. J. Higham, *Accuracy and Stability of Numerical Algorithms*, SIAM, 2002.
- [27] Y. Saad, A flexible inner-outer preconditioned GMRES algorithm, *SIAM Journal on Scientific Computing* 14 (2) (1993) 461–469.
- [28] Y. Saad, ILUT: A dual threshold incomplete LU factorization, *Numerical Linear Algebra with Applications* 1 (4) (1994) 387–402.
- [29] G. H. McKinley, Steady and transient motion of spherical particles in viscoelastic liquids, *Transport Processes in Bubble, Drops, and Particles* (2002) 338–375.
- [30] W. J. Lunsman, L. Genieser, R. C. Armstrong, R. A. Brown, Finite element analysis of steady viscoelastic flow around a sphere in a tube: calculations with constant viscosity models, *Journal of Non-Newtonian Fluid Mechanics* 48 (1) (1993) 63–99.
- [31] R. G. Owens, T. N. Phillips, Steady viscoelastic flow past a sphere using spectral elements, *International Journal for Numerical Methods in Engineering* 39 (9) (1996) 1517–1534.
- [32] C. Chauvière, R. G. Owens, How accurate is your solution?: Error indicators for viscoelastic flow calculations, *Journal of Non-Newtonian Fluid Mechanics* 95 (1) (2000) 1–33.
- [33] Y. Fan, Limiting behavior of the solutions of a falling sphere in a tube filled with viscoelastic fluids, *Journal of Non-Newtonian Fluid Mechanics* 110 (2) (2003) 77–102.
- [34] C. T. Kelley, *Iterative Methods for Linear and Nonlinear Equations*, SIAM, 1995.
- [35] P. Y. Huang, H. H. Hu, D. D. Joseph, Direct simulation of the sedimentation of elliptic particles in Oldroyd-B fluids, *Journal of Fluid Mechanics* 362 (1998) 297–325.
- [36] H. Lamb, *Hydrodynamics*, Cambridge University Press, 1932.
- [37] S. Boyaval, T. Lelièvre, C. Mangoubi, Free-energy-dissipative schemes for the Oldroyd-B model, *ESAIM: Mathematical Modelling and Numerical Analysis* 43 (03) (2009) 523–561.
- [38] N. Masmoudi, Global existence of weak solutions to macroscopic models of polymeric flows, *Journal de mathématiques pures et appliquées* 96 (5) (2011) 502–520.
- [39] J. W. Barrett, S. Boyaval, Existence and approximation of a (regularized) Oldroyd-B model, *Mathematical Models and Methods in Applied Sciences* 21 (09) (2011) 1783–1837.